


Zircon U–Pb dating of eclogite from the Qiangtang terrane, north-central Tibet: a case of metamorphic zircon with magmatic geochemical features

Qing-guo Zhai¹  · Bor-ming Jahn² · Xian-hua Li³ · Ru-yuan Zhang² · Qiu-li Li³ · Ya-nan Yang³ · Jun Wang¹ · Tong Liu³ · Pei-yuan Hu¹ · Suo-han Tang¹

Received: 26 March 2016 / Accepted: 14 October 2016 / Published online: 31 October 2016
© Springer-Verlag Berlin Heidelberg 2016

Abstract Zircon is probably the most important mineral used in the dating formation of high-pressure (HP) and ultrahigh-pressure (UHP) metamorphic rocks. The origin of zircon, i.e., magmatic or metamorphic, is commonly assessed by its external morphology, internal structure, mineral inclusions, Th/U ratios and trace element composition. In this study, we present an unusual case of metamorphic zircon from the Qiangtang eclogite, north-central Tibet. The zircon grains contain numerous eclogite-facies mineral inclusions, including omphacite, phengite, garnet and rutile; hence, they are clearly of metamorphic origin. However, they display features similar to common magmatic zircon, including euhedral crystal habit, high Th/U ratios and enriched heavy rare earth elements pattern. We suggest that these zircon grains formed from a different reservoir from that for garnet where no trace elements was present and trace element equilibrium between zircon and garnet was achieved. U–Pb dating of zircon gave an age of 232–237 Ma for the eclogite, and that of rutile yielded a slightly younger age of ca. 217 Ma. These ages are consistent with the reported Lu–Hf mineral isochron and phengite Ar–Ar ages. The zircon U–Pb and mineral Lu–Hf isochron

ages are interpreted as the time of the peak eclogite-facies metamorphism, whereas the rutile U–Pb and phengite Ar–Ar ages represent the time of exhumation to the middle crust. Thus, the distinction between metamorphic and magmatic zircons cannot be made using only Th/U ratios and heavy REE compositions for HP–UHP metamorphic rocks of oceanic derivation.

Keywords Tibet · Qiangtang · Eclogite · Oceanic derivation · Zircon origin · Rutile · U–Pb dating

Introduction

With the development of the SIMS (Secondary Ion Mass Spectrometry) U–Th–Pb analytical techniques, zircon has become probably the most important mineral used to constrain the metamorphic history of the HP–UHP metamorphic rocks (e.g., Gebauer 1996; Hoskin and Schaltegger 2003; Rubatto and Hermann 2007; Zheng et al. 2009; Liu and Liou 2011). In general, the identification of zircon as magmatic or metamorphic is commonly made by its external morphology, internal structure, Th/U ratios, trace element composition and mineral inclusions (e.g., Hoskin and Black 2000; Rubatto 2002; Corfu et al. 2003; Hoskin and Schaltegger 2003). Magmatic zircon grains are usually euhedral; they show internal oscillatory zoning, have Th/U ratios generally higher than 0.1 and exhibit enriched heavy REE. By contrast, metamorphic zircon grains are commonly anhedral, have lower Th/U ratios (<0.1) and relatively flat heavy REE, especially in garnet-bearing rocks (e.g., Hoskin and Black 2000; Rubatto 2002; Hoskin and Schaltegger 2003). However, these rules of identification have been debated, because the shape and contents of Th, U and REE of metamorphic zircon may be controlled by

Electronic supplementary material The online version of this article (doi:10.1007/s00531-016-1418-9) contains supplementary material, which is available to authorized users.

✉ Qing-guo Zhai
zhaiqingguo@126.com

¹ Institute of Geology, Chinese Academy of Geological Sciences, 26 Baiwanzhuang Road, Beijing 100037, China

² Department of Geosciences, National Taiwan University, Taipei 106, Taiwan

³ Institute of Geology and Geophysics, Chinese Academy of Sciences, Beijing 100029, China

many factors, such as the chemical composition of the metamorphic fluids, concurrent growth of minerals and growth velocity of zircon (Rowley et al. 1997; Vavra et al. 1999; Rubatto and Hermann 2003; Wu and Zheng 2004).

In this study, we present details of unusual metamorphic zircon grains from the Qiangtang eclogite from north-central Tibet to exposure such a problem in the genetic identification. These zircon grains are euhedral, have high Th/U ratios and enriched heavy REE compositions. Therefore, they fall in the category of magmatic zircon. In this work, we used two analytical methods, SIMS and LA-ICPMS (Laser Ablation Inductively Coupled Plasma Mass Spectrometry) techniques, to obtain the age, trace element abundances and oxygen isotopic compositions of the zircon grains. The data, together with the rutile U–Pb age, will be used to discuss the genesis of the zircon grains and the

geodynamic implications for the formation of the Qiangtang HP metamorphic belt.

Geologic background of the Qiangtang eclogite

The Qiangtang terrane lies in the north-central Tibetan plateau, bounded by the Jinsha suture to the north and the Bangong–Nujiang suture to the south (Fig. 1; e.g., BGMR 1993; Yin and Harrison 2000; Zhu et al. 2013). A >500 km HP metamorphic belt occurs in the middle of the Qiangtang terrane, and it is composed of a tectonic mélange of blueschist, eclogite, ophiolitic mélange and metasedimentary rocks (Li et al. 1995, 2006a, b; Kapp et al. 2003; Pullen et al. 2008; Zhai et al. 2011a, b, 2013a, b, c; Liang et al. 2012). The Qiangtang terrane is further subdivided into the South and North Qiangtang sub-terrane (Fig. 1). The Paleozoic rocks (Ordovician to Permian) in the South Qiangtang sub-terrane comprise metapelite, marble, sandstone, limestone and glaciomarine deposits. The glaciomarine deposits and cold-water biota suggest that the South Qiangtang sub-terrane has a Gondwana affinity (BGMR 1993; Li and Zheng 1993; Li et al. 1995; Jin 2002; Zhang et al. 2009). On the other hand, the Paleozoic rocks in the North Qiangtang sub-terrane are composed of Devonian, Carboniferous and Permian strata. They are mainly sandstone, mudstone and limestone, associated with fusulinid, coral and gigantopterid fossils of a Cathaysian affinity (BGMR 1993; Li and Zheng 1993; Li et al. 1995; Jin 2002; Zhang et al. 2009).

The Gemu eclogite is located in the middle of the Qiangtang HP metamorphic belt (Fig. 1). It occurs as blocks and/or lenses in marble and garnet–phengite schist, with mineral assemblages of garnet, omphacite, rutile, phengite, and minor quartz, epidote and titanite (Fig. 2a,

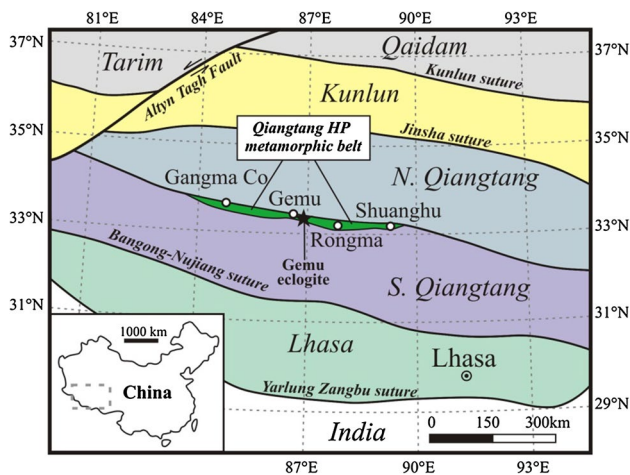


Fig. 1 Tectonic framework of the Tibetan plateau, showing the location of the Gemu eclogite

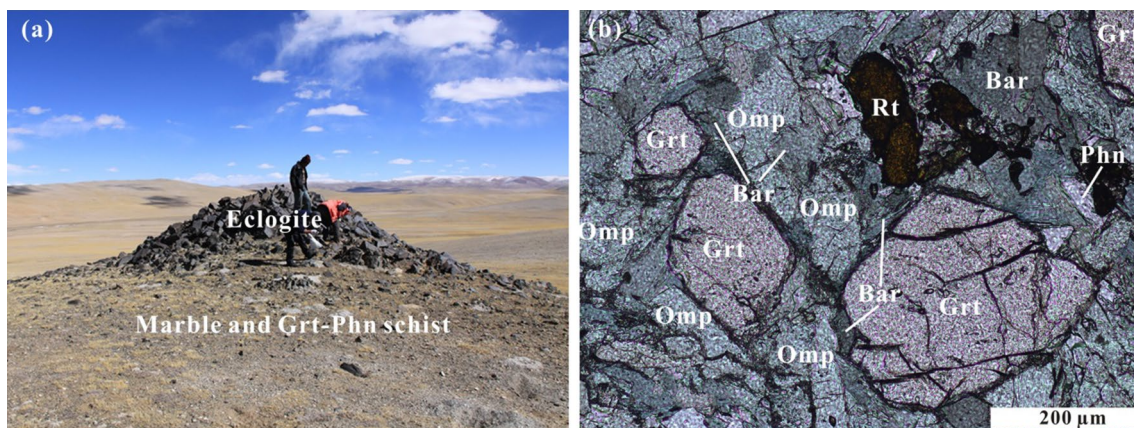


Fig. 2 Photograph (a) and Photomicrograph (b) of the Qiangtang eclogite (E0901). Mineral abbreviations are after Kretz (1983), except Phn for phengite and Bar for barroisite

b). Thermobarometric studies showed that the peak eclogite metamorphic condition was ~ 500 °C and ~ 2.2 GPa (Li et al. 2006b; Zhai et al. 2011a, b). This kind of low-temperature eclogite is consistent with its oceanic origin (Zhai et al. 2011a). Published zircon U–Pb ages of 230–237 Ma (Zhai et al. 2011b) and Lu–Hf mineral isochron ages of 233–244 Ma (Pullen et al. 2008) have been interpreted as the time of the peak eclogite-facies metamorphism, whereas phengite Ar–Ar ages of 214–219 Ma were considered to date time of the exhumation (Li et al. 2006a; Zhai et al. 2011b).

In this study, four eclogite samples (E0814, E0901, E0902 and E0903) were collected from the Gemu area in the central Qiangtang terrane (Fig. 1). They are from four massive eclogite blocks (>10 m), and their GPS localities are present in Table 1. The country rock of sample E0814 is marble, and those of samples E0901, E0902 and E0903 are garnet–phengite schists. These blocks are isolated, and they have sharp contact with the country rocks. Four eclogite samples have similar porphyroblastic texture, and they are composed of garnet (~ 40 vol.%), omphacite (~ 35 vol.%), phengite (<5 vol.%), rutile (~ 5 vol.%), and retrograded barroisite and actinolite (~ 10 vol.%), with or without quartz and albite.

Analytical methods

Mineral chemistry

The mineral compositions for inclusions in zircon from the eclogite were analyzed using an electron probe micro-analyzer (EPMA) JEOL JXA-8230 at the Institute of Mineral Resources, Chinese Academy of Geological Sciences. The operating conditions were 20 kV and 20 nA beam current with a 5- μ m probe diameter. Ferric iron in garnet and clinopyroxene was determined using the method of Droop (1987) and assuming $\text{Fe}^{3+} = \text{Na} - \text{Al} - \text{Cr}$ of Cawthorn and Collerson (1974). Fe^{3+} in amphibole was estimated on the basis of structural formulae of 23 oxygens following the charge balance method of Robinson et al. (1982). The results are listed in Supplementary Material 1.

SIMS zircon U–Pb analysis

Zircons were separated from four ca. 20 kg samples using conventional heavy liquid and magnetic separation techniques at the Special Laboratory of the Geological Team of Hebei Province, China. Zircon grains were further purified by handpicking under a binocular microscope. Zircon grains, together with zircon standard TEMORA and 91500 (Wiedenbeck et al. 1995; Black et al. 2004), were mounted

in epoxy mounts that were then polished to section the crystals in half for analysis. All zircons were documented in transmitted and reflected light, as well as by cathodoluminescence (CL) imaging to reveal their internal structures. CL images of zircons were obtained using a HITACH S-3000N scanning microscope fitted with a Gatan Chroma at Institute of Geology, Chinese Academy of Geological Sciences.

The mount was vacuum-coated with high-purity gold prior to SIMS analysis. Measurements of U, Th and Pb were conducted using a Cameca IMS-1280 SIMS at the Institute of Geology and Geophysics, Chinese Academy of Sciences in Beijing. The U–Th–Pb ratios and absolute abundances were determined relative to the standard zircon 91500 (Wiedenbeck et al. 1995), following operating and data processing procedures described by Li et al. (2009). The O_2^- primary ion beam was accelerated at 13 kV, with an intensity of ca. 8 nA. The ellipsoidal spot was about 20×30 μm in size. Positive secondary ions were extracted with a 10 kV potential. Oxygen flooding was used to increase the O_2 pressure to ca. 5×10^{-6} Torr in the sample chamber, enhancing the secondary Pb^+ sensitivity to a value of ca. 25 cps/nA/ppm for zircon.

In the secondary ion beam optics, a 60-eV energy window was used, together with a mass resolution of ca. 5400, to separate Pb^+ peaks from isobaric interferences. The field aperture was set to 7000 μm , and the transfer optic magnification was adjusted to 200. Rectangular lenses were activated in the secondary ion optics to increase the transmission at high mass resolution. A single electron multiplier was used in ion-counting mode to measure secondary ion beam intensities by peak jumping. Each measurement consists of 7 cycles, and the total analytical time was ca. 12 min.

Analyses of the standard zircon 91500 were interspersed with unknown grains. A long-term uncertainty of 1.5% (1 RSD) for $^{206}\text{Pb}/^{238}\text{U}$ measurements of the standard zircons was propagated to the unknowns (Li et al. 2010a, b, c), although the measured $^{206}\text{Pb}/^{238}\text{U}$ error in a specific session was generally around 1% (1 RSD) or less. Measured compositions were corrected for common Pb using measured non-radiogenic ^{204}Pb . Corrections are sufficiently small to be insensitive to the choice of common Pb composition, and an average of present-day crustal composition (Stacey and Kramers 1975) was used for the common Pb assuming that the common Pb is largely surface contamination introduced during sample preparation. Uncertainties on individual analyses in data tables are reported at the 1 σ level; mean ages for pooled U/Pb analyses are quoted at the 95% confidence interval. Data reduction was carried out using the ISOPLOT program (Ludwig 2001) and is listed in Table 1.

Table 1 SIMS U–Pb and O isotopic data for zircons from the Qiangtang eclogite

Sample spot	U (ppm)	Th (ppm)	Pb (ppm)	Tb/U	$^{206}\text{Pb}/^{204}\text{Pb}_m$	$f_{206}\%$	$^{207}\text{Pb}/^{235}\text{U}$ ±1σ (%)	$^{206}\text{Pb}/^{238}\text{U}$ ±1σ (%)	$^{207}\text{Pb}/^{206}\text{Pb}$ ±1σ (%)	$t_{207/206}$ (Ma)	±σ	$t_{206/238}$ (Ma)	±σ	$t_{207/235}$ (Ma)	±σ	$\delta^{18}\text{O}$ (‰)	2σ				
E0814, eclogite, Lat. 33°38.522', Long. 86°35.521'																					
E0814-1	877	1354	50	1.54	9785	0.19	0.25698	2.20	0.0377	1.54	0.70016	0.04948	1.57	170.5	36.3	232.2	4.6	238.4	3.6	5.24	0.25
E0814-2	834	1244	47	1.49	60,862	0.03	0.26447	2.04	0.0376	1.52	0.74388	0.05107	1.37	244.1	31.2	238.3	4.3	237.7	3.5	5.26	0.38
E0814-3	206	225	10	1.09	4416	0.42	0.25399	4.96	0.0370	1.51	0.30376	0.04983	4.72	187.0	106.4	229.8	10.2	234.0	3.5	5.38	0.18
E0814-4	725	1467	46	2.02	17,466	0.11	0.26292	2.28	0.0380	1.51	0.66193	0.05015	1.71	202.1	39.2	237.0	4.8	240.6	3.6	5.35	0.13
E0814-5	486	509	25	1.05	5294	0.35	0.25757	2.82	0.0376	1.50	0.53174	0.04974	2.39	182.8	54.7	232.7	5.9	237.7	3.5	4.91	0.16
E0814-6	162	151	8	0.94	20,185	0.09	0.26683	5.32	0.0377	1.53	0.28833	0.05134	5.10	256.2	113.1	240.2	11.4	238.5	3.6	5.15	0.24
E0814-7	219	224	11	1.02			0.27317	2.98	0.0376	1.54	0.51782	0.05271	2.55	316.3	56.9	245.2	6.5	237.9	3.6	5.44	0.26
E0814-8	605	924	35	1.53	12,323	0.15	0.26323	2.74	0.0380	1.50	0.54863	0.05022	2.29	205.3	52.3	237.3	5.8	240.5	3.5	4.68	0.33
E0814-9	711	1191	41	1.68	32,834	0.06	0.25489	2.20	0.0369	1.52	0.69094	0.05008	1.59	198.8	36.6	230.5	4.6	233.7	3.5	5.19	0.25
E0814-10	708	1164	42	1.64	34,320	0.05	0.27132	2.74	0.0384	1.53	0.55823	0.05131	2.28	254.7	51.5	243.7	6.0	242.6	3.6	5.11	0.27
E0814-11	332	373	16	1.12	6829	0.27	0.25035	3.21	0.0350	1.50	0.46714	0.05193	2.84	282.4	63.8	226.9	6.6	221.5	3.3	4.86	0.37
E0814-12	670	1176	40	1.76	24,414	0.08	0.27881	2.44	0.0381	1.51	0.61803	0.05314	1.92	334.8	42.9	249.7	5.4	240.7	3.6	4.91	0.25
E0814-13	270	261	14	0.97	15,630	0.12	0.25750	3.55	0.0369	1.52	0.42680	0.05058	3.21	221.9	72.7	232.7	7.4	233.7	3.5	5.54	0.22
E0814-14	885	1844	56	2.08	3524	0.53	0.25573	2.64	0.0375	1.50	0.56892	0.04945	2.17	169.1	50.0	231.2	5.5	237.4	3.5	5.23	0.26
E0814-15	346	359	17	1.04	6053	0.31	0.27080	3.92	0.0367	1.50	0.38334	0.05353	3.62	351.5	79.9	243.3	8.5	232.3	3.4	4.56	0.30
E0814-16	898	1560	54	1.74	15,631	0.12	0.26683	2.07	0.0377	1.54	0.74113	0.05136	1.39	257.0	31.7	240.2	4.4	238.4	3.6	5.00	0.29
E0814-17	260	278	13	1.07	3453	0.54	0.25087	4.24	0.0362	1.54	0.36282	0.05023	3.95	205.6	89.1	227.3	8.7	229.4	3.5	5.47	0.23
E0814-18	913	1931	59	2.12	108,394	0.02	0.27528	1.99	0.0382	1.50	0.75246	0.05222	1.31	295.0	29.7	246.9	4.4	241.9	3.6	4.93	0.26
E0814-19	677	1314	40	1.94	9236	0.20	0.24373	2.53	0.0359	1.51	0.59629	0.04923	2.03	158.8	46.9	221.5	5.1	227.4	3.4	5.50	0.28
E0814-20	853	1735	54	2.03	19,546	0.10	0.26900	2.26	0.0382	1.51	0.66904	0.05107	1.68	244.0	38.2	241.9	4.9	241.7	3.6	4.81	0.23
E0814-21	680	1099	39	1.62	19,083	0.10	0.26731	2.63	0.0375	1.51	0.57360	0.05164	2.16	269.6	48.7	240.5	5.7	237.6	3.5	5.66	0.25
E0814-22	944	1691	57	1.79	26,464	0.07	0.26752	2.04	0.0381	1.52	0.74478	0.05088	1.36	235.6	31.1	240.7	4.4	241.2	3.6	5.01	0.35
E0814-23	340	437	19	1.29	6059	0.31	0.25606	3.30	0.0382	1.58	0.47952	0.04868	2.90	132.2	66.8	231.5	6.9	241.4	3.8	5.07	0.31
E0901, eclogite, Lat. 33°28.625', Long. 86°02.750'																					
E0901-1	727	1058	41	1.46	22,411	0.08	0.26776	2.19	0.0373	1.51	0.68620	0.05203	1.60	286.6	36.1	240.9	4.7	236.2	3.5	5.08	0.25
E0901-2	1144	2045	67	1.79	18,845	0.10	0.25683	1.94	0.0367	1.50	0.77274	0.05074	1.23	229.0	28.2	232.1	4.0	232.4	3.4	5.10	0.30
E0901-3	801	1050	43	1.31	15,039	0.12	0.26049	2.62	0.0370	1.51	0.57662	0.05107	2.14	244.1	48.6	235.1	5.5	234.2	3.5	4.84	0.27
E0901-4	934	1498	54	1.60	6275	0.30	0.25702	2.21	0.0378	1.51	0.68256	0.04936	1.61	164.9	37.3	232.3	4.6	239.0	3.5	5.00	0.23
E0901-5	952	1431	55	1.50	21,044	0.09	0.27380	2.02	0.0382	1.54	0.76218	0.05203	1.31	286.5	29.7	245.7	4.4	241.5	3.7	5.00	0.13
E0901-6	747	1546	48	2.07	29,138	0.06	0.26785	2.08	0.0382	1.50	0.72265	0.05092	1.44	237.2	32.8	241.0	4.5	241.4	3.6	5.40	0.22
E0901-7	219	185	10	0.84	4922	0.38	0.24164	4.83	0.0350	1.54	0.31769	0.05002	4.58	195.9	103.1	219.8	9.6	222.0	3.4	5.61	0.19
E0901-8	820	1239	47	1.51	17,898	0.10	0.26449	2.08	0.0377	1.50	0.72170	0.05091	1.44	237.0	32.9	238.3	4.4	238.4	3.5	5.18	0.23
E0901-9	554	868	32	1.57	16,805	0.11	0.27400	2.47	0.0381	1.53	0.61996	0.05219	1.94	293.6	43.7	245.9	5.4	240.9	3.6	5.35	0.27
E0901-10	1230	2116	74	1.72	6941	0.27	0.26375	2.10	0.0379	1.50	0.71372	0.05053	1.47	219.4	33.8	237.7	4.5	239.5	3.5	5.24	0.17
E0901-11	353	406	17	1.15	6854	0.27	0.23703	3.17	0.0341	1.56	0.49168	0.05038	2.76	212.4	62.8	216.0	6.2	216.3	3.3	5.28	0.29
E0901-12	142	129	7	0.91	3217	0.58	0.26217	5.10	0.0360	1.53	0.29969	0.05289	4.86	323.9	106.8	236.4	10.8	227.7	3.4	4.99	0.35
E0901-13	1060	2133	66	2.01	13,162	0.14	0.25297	2.06	0.0371	1.51	0.73068	0.04949	1.41	171.1	32.5	229.0	4.2	234.7	3.5	5.25	0.30
E0901-14	706	751	36	1.06	13,023	0.14	0.27222	2.29	0.0375	1.52	0.66458	0.05259	1.71	311.2	38.5	244.5	5.0	237.6	3.5	5.01	0.25

Table 1 continued

Sample spot	U (ppm)	Th (ppm)	Pb (ppm)	Tb/U	$^{206}\text{Pb}/^{204}\text{Pb}_m$	f_{206} %	$^{207}\text{Pb}/^{235}\text{U}$	$\pm 1\sigma$ (%)	$^{206}\text{Pb}/^{238}\text{U}$	$\pm 1\sigma$ (%)	ρ	$^{207}\text{Pb}/^{206}\text{Pb}$	$\pm 1\sigma$ (%)	$t_{507/206}$ (Ma)	$\pm \sigma$	$t_{307/235}$ (Ma)	$\pm \sigma$	$t_{306/238}$ (Ma)	$\pm \sigma$	$\delta^{18}\text{O}$ (‰)	2σ
E0901-15	902	1775	58	1.97	14,052	0.13	0.26848	2.10	0.0385	1.50	0.71389	0.05063	1.47	224.0	33.7	241.5	4.5	243.3	3.6	5.34	0.20
E0901-16	1279	1717	70	1.34	19,464	0.10	0.26494	1.92	0.0372	1.51	0.78325	0.05167	1.20	271.0	27.2	238.6	4.1	235.4	3.5	5.13	0.28
E0901-17	1653	2521	93	1.52	25,699	0.07	0.26170	1.84	0.0370	1.50	0.81737	0.05130	1.06	254.5	24.1	236.0	3.9	234.2	3.5	4.79	0.23
E0901-18	1118	1946	66	1.74	56,525	0.03	0.26676	1.91	0.0379	1.50	0.78533	0.05108	1.18	244.3	27.1	240.1	4.1	239.7	3.5	5.42	0.30
E0901-19	789	1083	45	1.37	11,061	0.17	0.26853	2.23	0.0383	1.50	0.67433	0.05090	1.65	236.5	37.5	241.5	4.8	242.0	3.6	5.44	0.32
E0901-20	708	1338	43	1.89	9254	0.20	0.25882	2.32	0.0377	1.52	0.65466	0.04976	1.76	183.9	40.4	233.7	4.9	238.7	3.6	5.50	0.26
E0901-21	831	1563	51	1.88	12,099	0.15	0.26405	2.48	0.0379	1.51	0.60866	0.05058	1.96	221.5	44.8	237.9	5.3	239.6	3.5	5.15	0.29
E0901-22	1015	1868	61	1.84	18,316	0.10	0.26822	2.20	0.0378	1.51	0.68770	0.05152	1.60	264.3	36.3	241.3	4.7	238.9	3.6	4.76	0.27
E0901-23	1044	2066	65	1.98	21,287	0.09	0.26225	2.01	0.0377	1.50	0.74729	0.05047	1.33	216.8	30.6	236.5	4.2	238.5	3.5	4.89	0.27
E0901-24	671	1041	39	1.55	2013	0.93	0.25795	3.08	0.0381	1.51	0.48854	0.04913	2.69	154.0	61.8	233.0	6.4	240.9	3.6	5.51	0.19
E0901-25	407	429	21	1.05	4952	0.38	0.24890	3.39	0.0372	1.52	0.44707	0.04853	3.04	125.1	70.0	225.7	6.9	235.4	3.5	4.90	0.20
E0901-26	784	1266	46	1.62	9576	0.20	0.26181	2.37	0.0382	1.50	0.63306	0.04968	1.84	180.0	42.3	236.1	5.0	241.8	3.6	4.68	0.27
E0902, eclogite, Lat. 33°24.936', Long. 86°28.171'																					
E0902-1	1749	2910	104	1.66	32,410	0.06	0.27245	1.78	0.0385	1.50	0.84409	0.05139	0.95	258.3	21.7	244.7	3.9	243.2	3.6	4.12	0.34
E0902-2	765	1491	48	1.95	15,022	0.12	0.26945	2.18	0.0377	1.50	0.68760	0.05180	1.58	276.5	35.9	242.3	4.7	238.7	3.5	5.45	0.36
E0902-3	892	1246	49	1.40	4229	0.44	0.26035	2.61	0.0373	1.50	0.57560	0.05057	2.14	221.3	48.7	234.9	5.5	236.3	3.5	5.40	0.33
E0902-4	1124	1974	67	1.76	16,255	0.12	0.26576	1.97	0.0378	1.51	0.76429	0.05100	1.27	240.7	29.0	239.3	4.2	239.2	3.5	4.99	0.42
E0902-5	983	1769	58	1.80	10,719	0.17	0.25819	2.09	0.0367	1.51	0.72099	0.05106	1.45	243.7	33.0	233.2	4.4	232.2	3.4	5.02	0.36
E0902-6	687	1305	42	1.90	9991	0.19	0.26175	2.37	0.0375	1.50	0.63357	0.05058	1.83	221.6	41.8	236.1	5.0	237.5	3.5	4.66	0.26
E0902-7	649	981	37	1.51	6276	0.30	0.26459	2.78	0.0375	1.53	0.55133	0.05116	2.32	248.2	52.5	238.4	5.9	237.4	3.6	4.48	0.41
E0902-8	385	424	19	1.10	5852	0.32	0.25968	3.28	0.0357	1.53	0.46449	0.05277	2.91	318.9	64.8	234.4	6.9	226.1	3.4	4.31	0.26
E0902-9	528	893	30	1.69	2780	0.67	0.26292	3.77	0.0366	1.54	0.40867	0.05214	3.44	291.5	76.7	237.0	8.0	231.6	3.5	4.73	0.38
E0902-10	636	1015	37	1.60	9521	0.20	0.26592	2.34	0.0383	1.51	0.64348	0.05035	1.79	211.4	41.1	239.4	5.0	242.3	3.6	4.55	0.27
E0902-11	644	790	34	1.23	10,711	0.17	0.26111	2.30	0.0368	1.51	0.65349	0.05141	1.74	259.1	39.6	235.6	4.9	233.2	3.4	4.37	0.27
E0902-12	232	229	12	0.99	4371	0.43	0.26753	3.75	0.0378	1.54	0.41027	0.05137	3.42	257.4	76.8	240.7	8.1	239.0	3.6	4.77	0.33
E0902-13	1894	3750	121	1.98	41,516	0.05	0.27244	1.75	0.0386	1.50	0.85664	0.05120	0.91	249.7	20.7	244.6	3.8	244.1	3.6	4.89	0.28
E0902-14	820	1725	53	2.10	15,679	0.12	0.26837	2.34	0.0385	1.50	0.64112	0.05055	1.80	220.3	41.0	241.4	5.0	243.6	3.6	5.32	0.29
E0902-15	563	788	29	1.40	12,488	0.15	0.24287	3.30	0.0346	1.60	0.48282	0.05088	2.89	235.4	65.4	220.8	6.6	219.4	3.4	4.41	0.30
E0902-16	440	423	22	0.96	9121	0.21	0.24737	3.00	0.0369	1.50	0.50010	0.04857	2.60	127.2	60.0	224.4	6.1	233.8	3.4	4.96	0.16
E0902-17	817	1233	46	1.51	5509	0.34	0.26229	2.49	0.0371	1.50	0.60189	0.05122	1.99	250.6	45.2	236.5	5.3	235.1	3.5	5.23	0.26
E0902-18	922	1467	53	1.59	18,696	0.10	0.26426	2.05	0.0374	1.51	0.73377	0.05129	1.40	253.7	31.8	238.1	4.4	236.5	3.5	4.92	0.29
E0902-19	1123	2370	72	2.11	14,4620	0.01	0.27595	1.89	0.0377	1.50	0.79424	0.05302	1.15	329.6	25.9	247.4	4.2	238.9	3.5	4.78	0.23
E0902-20	757	1404	45	1.85	22,058	0.08	0.26427	2.14	0.0373	1.53	0.71277	0.05134	1.50	256.1	34.2	238.1	4.6	236.3	3.5	5.16	0.39
E0903, eclogite, Lat. 33°15.159', Long. 86°19.291'																					
E0903-1	1477	2856	91	1.93	6331	0.30	0.26325	2.42	0.0379	1.50	0.62148	0.05042	1.89	214.5	43.3	237.3	5.1	239.6	3.5	4.82	0.26
E0903-2	901	1560	50	1.73	9215	0.20	0.25057	2.37	0.0355	1.55	0.65272	0.05121	1.80	250.1	40.8	227.0	4.8	224.8	3.4	4.63	0.26
E0903-3	182	166	9	0.91	1946	0.96	0.25140	4.75	0.0377	1.60	0.33655	0.04837	4.47	117.4	102.2	227.7	9.7	238.5	3.7	4.09	0.22
E0903-4	952	1252	50	1.31	5519	0.34	0.25488	2.34	0.0359	1.51	0.64398	0.05153	1.79	264.6	40.6	230.5	4.8	227.2	3.4	5.09	0.23
E0903-5	898	1619	52	1.80	12,818	0.15	0.25551	2.40	0.0363	1.52	0.63145	0.05101	1.86	241.5	42.4	231.0	5.0	230.0	3.4	5.80	0.45

Table 1 continued

Sample spot	U (ppm)	Th (ppm)	Pb (ppm)	Th/U	$^{206}\text{Pb}/^{204}\text{Pb}_m$	$f_{206}\%$	$^{207}\text{Pb}/^{235}\text{U}$	$\pm 1\sigma$ (%)	$^{206}\text{Pb}/^{238}\text{U}$	$\pm 1\sigma$ (%)	ρ	$^{207}\text{Pb}/^{206}\text{Pb}$	$\pm 1\sigma$ (%)	$t_{507/206}$ (Ma)	$\pm 1\sigma$	$t_{507/235}$ (Ma)	$\pm 1\sigma$	$t_{506/238}$ (Ma)	$\pm 1\sigma$	$\delta^{18}\text{O}$ (‰)	2σ
E0903-6	579	734	30	1.27	2949	0.63	0.25267	3.09	0.0356	1.52	0.49111	0.05144	2.69	260.5	60.6	228.7	6.3	225.7	3.4	4.45	0.30
E0903-7	852	1246	46	1.46	4381	0.43	0.24795	2.81	0.0361	1.54	0.54959	0.04977	2.35	184.3	53.8	224.9	5.7	228.8	3.5	4.91	0.40
E0903-8	1516	3422	97	2.26	14,145	0.13	0.25653	1.95	0.0369	1.55	0.79614	0.05041	1.18	213.7	27.1	231.9	4.1	233.7	3.6	5.64	0.33
E0903-9	511	723	27	1.41	2482	0.75	0.25733	4.48	0.0366	1.52	0.33905	0.05096	4.22	238.9	94.4	232.5	9.4	231.9	3.5	4.74	0.17
E0903-10	985	1562	58	1.59	15,286	0.12	0.26821	2.29	0.0381	1.54	0.67004	0.05109	1.70	245.0	38.7	241.3	4.9	240.9	3.6	5.03	0.30
E0903-11	274	275	14	1.00	3693	0.51	0.26143	3.77	0.0364	1.54	0.40955	0.05204	3.44	287.4	76.7	235.8	8.0	230.7	3.5	4.95	0.21
E0903-12	732	1427	45	1.95	9099	0.21	0.25588	2.36	0.0379	1.53	0.64847	0.04901	1.79	148.2	41.5	231.3	4.9	239.6	3.6	3.89	0.25
E0903-13	949	1393	54	1.47	2790	0.67	0.26903	3.59	0.0376	1.51	0.41907	0.05188	3.26	280.1	73.0	241.9	7.8	238.0	3.5	4.75	0.33
E0903-14	513	564	26	1.10	5779	0.32	0.25545	2.98	0.0363	1.50	0.50505	0.05109	2.57	244.9	58.2	231.0	6.2	229.6	3.4	4.69	0.24
E0903-15	910	1117	45	1.23	4480	0.42	0.24369	2.58	0.0349	1.50	0.58098	0.05068	2.10	226.4	47.9	221.4	5.2	221.0	3.3	5.03	0.33
E0903-16	986	1260	54	1.28	6174	0.30	0.26752	2.37	0.0380	1.50	0.63398	0.05112	1.83	246.4	41.7	240.7	5.1	240.1	3.5	5.17	0.31
E0903-17	1430	2079	81	1.45	29,232	0.06	0.26161	2.05	0.0381	1.50	0.73034	0.04985	1.40	188.2	32.3	236.0	4.3	240.8	3.5	4.77	0.27
E0903-18	710	1099	41	1.55	3799	0.49	0.26158	2.80	0.0378	1.53	0.54693	0.05022	2.34	205.1	53.5	235.9	5.9	239.0	3.6	4.71	0.34
E0903-19	979	1325	51	1.35	6846	0.27	0.25269	2.49	0.0356	1.50	0.60367	0.05144	1.99	260.6	45.0	228.8	5.1	225.7	3.3	4.66	0.31
E0903-20	1192	2083	68	1.75	31,316	0.06	0.25789	2.38	0.0363	1.50	0.63064	0.05147	1.85	261.9	41.9	233.0	5.0	230.1	3.4	4.40	0.29

The value of $^{206}\text{Pb}/^{204}\text{Pb}_m$ is the measured value. f_{206} is the percentage of common ^{206}Pb in total ^{206}Pb

SIMS rutile U–Pb analysis

Measurements of U, Th and Pb were conducted using the Cameca IMS-1280 SIMS at the Institute of Geology and Geophysics, Chinese Academy of Sciences in Beijing. The analytical procedures were similar to those reported by Li et al. (2011). Rutile crystals were mounted in epoxy together with the R10 rutile standard (concordia age = 1090 ± 5 Ma; Luvizotto et al. 2009), 99JHQ-1 rutile ($^{206}\text{Pb}/^{238}\text{U}$ age = 218 ± 1.2 Ma; Li et al. 2003) and an in-house rutile megacrystal standard (JDX) ($^{207}\text{Pb}/^{206}\text{Pb}$ age = 521 Ma, $^{206}\text{Pb}/^{238}\text{U}$ age = 500–520 Ma; unpublished TIMS data). The mount was polished to expose the interior of the crystals. After thorough cleaning, the mount was vacuum-coated with high-purity gold prior to ion probe analysis.

The O_2^- primary ion beam was accelerated at 13 kV, with an intensity of ca. 15 nA. The aperture illumination mode (Kohler illumination) was used with a ca. 200- μm aperture to produce even sputtering over the entire analyzed area. The ellipsoidal spot was about $20 \times 30 \mu\text{m}$ in size. Positive secondary ions were extracted with a 10-kV potential. A mass resolution of ~ 6000 was used and the magnet was cyclically peak-stepped though a sequence including $^{206}\text{Pb}^+$, $^{207}\text{Pb}^+$, $^{208}\text{Pb}^+$, U^+ , UO^+ , ThO^+ , UO_2^+ and $^{49}\text{TiO}_4^+$ to produce one set of data. A single ion-counting electron multiplier (EM) was used as the detection device. The $^{49}\text{TiO}_4^+$ signal was used as the reference peak for centering secondary ion beams because this peak has a strong enough intensity and is free of interference from ZrO. Each measurement consisted of 10 cycles, and the total analytical time was ~ 15 min, including 2-min rastering prior to the actual analysis in order to reduce the contribution of surface contaminant Pb. The mass fractionations of Pb isotopes and Pb hydrides (requiring a mass resolution $>30,000$) were not considered because a number of studies have shown that these two effects are negligible and there appears to be a mutual cancelation (e.g., Williams 1998; Ireland and Williams 2003; Li et al. 2011).

In this study, R10 rutile was used as the primary standard. The calibration curve was constructed with a power law relationship between Pb/U and UO_2/U relative to the R10 rutile standard dated at 1090 ± 5 Ma (Luvizotto et al. 2009). The exponential E, shown as the slope in linear relationship between $\ln(\text{Pb}/\text{U})$ vs. $\ln(\text{UO}_2/\text{U})$, was finely tuned to correct the results of 99JHQ-1 rutile, which is dated at 218 ± 1.2 Ma by ID-TIMS (Li et al. 2003). The external reproducibility (3.4%, 1σ) obtained from the R10 standard rutile during the analytical session was propagated together with the precision of the unknowns to give an overall error for the $^{206}\text{Pb}/^{238}\text{U}$ ratio of individual analysis (Li et al. 2010a, b). As a quality-evidence, with the calibration curve, the in-house JDX rutile standard yielded an average U–Pb

age of 510 ± 8 Ma, which is consistent with the TIMS result (500–520 Ma). In addition, a rutile sample from a deposit located in the Hengshan Mountains, Shanxi Province, China, $^{207}\text{Pb}/^{206}\text{Pb}$ age = 1780 ± 10 Ma, $^{207}\text{Pb}/^{235}\text{U}$ age = 1779 ± 14 Ma and $^{206}\text{Pb}/^{238}\text{Pb}$ age = 1777 ± 10 Ma (Shi et al. 2012). Because the $^{207}\text{Pb}/^{206}\text{Pb}$ age is independent of calibration from inter-element fractionation, the concordance of U–Pb ages indicates a well-established calibration curve.

Though U, Th and Pb concentrations are not essential for rutile U–Pb dating, they are useful additional pieces of information for characterization and are always measured during ion microprobe analysis. In general, the U concentrations were calculated based on a ratio of $^+\text{UO}_{x(x=0,1,2)}$ and the intensity of matrix ions, such as $^{90}\text{Zr}_2\text{O}^+$ for zircon and $\text{CaTi}_2\text{O}_4^+$ for perovskite (Li et al. 2010b). However, we observed that the intensity of $^{49}\text{TiO}_4^+$ in rutile varied by up to 400% among different samples under the same analytical conditions. The cause of this phenomenon is unclear, but may be related to the crystal structure. Nevertheless, the method used for zircon or perovskite is unsuitable for rutile. In this study, we estimated the U concentrations by U^+ ion yield based on the R10 standard with 30 ppm U (Luvizotto et al. 2009). This method is proven to be effective to within 50% uncertainty by monitoring the JDX rutile megacrystal.

Rutile usually contains very low concentrations of Th making it favorable in U/Pb dating using the ^{208}Pb -based common Pb correction (Clark et al. 2000; Luvizotto et al. 2009). We observed that the ThO^+/UO^+ ratios (corresponding to Th/U with a factor of around 1; Williams 1998) in rutile standards are lower than 0.01, mostly $<1\text{E} - 4$. This feature of rutile is quite useful not only in U–Pb dating, but also in judging if it is rutile or another mineral. However, most of the dated rutile grains in eclogite contain so low U contents that the small Th content could not be ignored. So, the common Pb proportion was calculated by ^{207}Pb -based correction (Williams 1998). As for the age calculation, assuming that the rutiles are concordant in the U–Pb system, an alternative to the common-lead correction is to use the lower and upper intercepts of a regression line of the data points on a Tera–Wasserburg plot to calculate the U–Pb age and the common-lead composition, respectively (Williams 1998). The ^{207}Pb -based correction results using the terrestrial Pb isotope composition (Stacey and Kramers 1975) are listed for reference only due to the large uncertainties. Rutile U–Pb data are listed in Table 2.

Zircon trace element analysis

Trace elements in zircon were analyzed by LA-ICPMS at the Geologic Lab Center, China University of Geosciences (Beijing). The instrument couples a quadrupole ICPMS

(Agilent 7500a) and an UP-193 Solid-State laser (193 nm, New Wave Research Inc.) with the automatic positioning system. In this study, the laser spot size was set to $36 \mu\text{m}$, the laser energy density at $8.5 \text{ J}/\text{cm}^2$ and repetition rate at 10 Hz. The procedure of laser sampling is 5-s pre-ablation, 20-s sample-chamber flushing and 40-s sampling ablation. The ablated material is carried into the ICP-MS by the high-purity helium gas stream with a flux of 0.8 L/min. The whole laser path was fluxed with N_2 (15 L/min) and Ar (1.15 L/min) in order to increase energy stability. The counting time was 15 ms for all elements. Calibrations for zircon analyses were carried out using NIST 610 glass as an external standard and Si as internal standard. Trace element concentrations of zircons were calculated using GLITTER 4.0. Analyses of standards (GJ-1 and NIST 610) indicate that the precision (RSD%) is better than 10% (2σ). The results are listed in Supplementary Material 2.

SIMS O isotopic analysis

Zircon oxygen isotopes were measured using the same Cameca IMS 1280 SIMS at the Institute of Geology and Geophysics, Chinese Academy of Sciences in Beijing, with analytical procedures similar to those reported by Li et al. (2010a, b, c). The Cs^+ primary ion beam was accelerated at 10 kV, with an intensity of ca. 2 nA (Gaussian mode with a primary beam aperture of $200 \mu\text{m}$ to reduce aberrations) and rastered over a $10\text{-}\mu\text{m}$ area. The spot was about $20 \mu\text{m}$ in diameter ($10 \mu\text{m}$ beam diameter + $10 \mu\text{m}$ raster).

The normal-incidence electron flood gun was used to compensate for sample charging during analysis with homogeneous electron density over a $100\text{-}\mu\text{m}$ oval area. Negative secondary ions were extracted with a -10 kV potential. The field aperture was set to $5000 \mu\text{m}$, and the transfer-optics magnification was adjusted to give a field of view of $125 \mu\text{m}$ (FA = 8000). The energy slit width was 30 eV, and the mechanical position of the slit was controlled before starting the analysis (5 eV gap, -500 digits with respect to the maximum). The entrance slit width was $\sim 120 \mu\text{m}$ and the exit slit width for multicollector Faraday cups (FCs) for ^{16}O and ^{18}O was $500 \mu\text{m}$ (MRP = 2500). The intensity of ^{16}O was typically 1×10^9 cps. Oxygen isotopes were measured in multicollector mode using two off-axis Faraday cups. The NMR (Nuclear Magnetic Resonance) probe was used for magnetic field control with stability better than 2.5 ppm over 16 h on mass 17. One analysis took ~ 4 min, consisting of pre-sputtering (~ 120 s), automatic beam centering (~ 60 s) and integration of oxygen isotopes (10 cycles \times 4 s, total 40 s). Uncertainties on individual analyses are reported at the 1σ level. With low noise on the two FC amplifiers, the internal precision of a single analysis is generally better than 0.2‰ for the $^{18}\text{O}/^{16}\text{O}$ ratio. Values of $\delta^{18}\text{O}$ were standardized to Vienna

Standard Mean Ocean Water (VSMOW) and reported in standard per mil notation.

The instrumental mass fractionation factor (IMF) was corrected using 91500 zircon standard with $(\delta^{18}\text{O})_{\text{VSMOW}} = 9.9\text{‰}$ (Wiedenbeck et al. 2004). Measured $^{18}\text{O}/^{16}\text{O}$ ratios were normalized using VSMOW compositions ($^{18}\text{O}/^{16}\text{O} = 0.0020052$) and then corrected for the instrumental mass fractionation factor (IMF) as follows:

$$(\delta^{18}\text{O})_{\text{M}} = \left[\left(\frac{^{18}\text{O}}{^{16}\text{O}} \right)_{\text{M}} / 0.0020052 - 1 \right] \times 1000 (\text{‰})$$

$$\text{IMF} = (\delta^{18}\text{O})_{\text{M(standard)}} - (\delta^{18}\text{O})_{\text{vsmow}}$$

$$(\delta^{18}\text{O})_{\text{Sample}} = (\delta^{18}\text{O})_{\text{M}} + \text{IMF}$$

Thirty-four measurements of the TEMORA zircon standard yielded a weighed mean for $\delta^{18}\text{O}$ of $8.20 \pm 0.26\text{‰}$ (2σ), which is consistent with the reported value of 8.20‰ (Black et al. 2004). Zircon oxygen isotopic data are listed in Table 1.

Zircon description and mineral inclusions

Zircon grains from the Qiangtang eclogite are euhedral or subhedral and colorless, with sizes ranging from 50 to 100 μm . All grains show similar crystal forms with elongated and/or short prisms (Fig. 3). Most zircon grains have homogeneous CL images (Fig. 3a–d) and exhibit similar crystal forms with no inherited cores or resorption. Furthermore, some grains show high luminescent bright stripes (Fig. 3a–d).

The zircons grains contain many mineral inclusions of the eclogite-facies paragenesis, including omphacite, phengite, garnet and rutile (Fig. 3e–p). Most inclusions lie in the interior of zircon crystals, and they are not connected to the matrix through fractures (Fig. 3). This occurrence indicates that the inclusions are primary, not secondary inclusions of the zircon grains. The inclusions occur in various shapes and sizes (1–15 μm ; Fig. 3e–p). Small mineral inclusions (<5 μm) were identified using laser Raman spectroscopy. We also determined the chemical compositions of larger inclusions (>5 μm) using EPMA. A total of 31 mineral inclusions were analyzed, and their chemical compositions are listed in Supplementary Material 1. Garnet is rich in almandine and grossular, but poor in pyrope and spessartine ($\text{Alm}_{56.7-57.7}\text{Prp}_{14.6-15.9}\text{Grs}_{25.8-25.9}\text{Sps}_{1.4-1.5}$). The jadeite component of omphacite ranges from 32 to 39 mol%.

Phengite inclusions are numerous within the zircons, and they are characterized by high Si-values (3.30–3.52 pfu) when normalized to 11 oxygen. Thus, the geochemical features of mineral inclusions are consistent with those of the matrix minerals in the Qiangtang eclogite (Garnet: $\text{Alm}_{57-78}\text{Prp}_{2-9}\text{Grs}_{8-33}\text{Sps}_{0-8}$, Omphacite: 30–42 mol% jadeite, Phengite: 3.35–3.48 Si-content) (Zhai et al. 2011a, b).

U–Pb geochronology

In order to clarify the issue of the peak metamorphic age or exhumation time of the Qiangtang eclogite, we dated four eclogite samples (E0814, E0901, E0902 and E0903) using the SIMS U–Pb technique (Table 1). Furthermore, we also dated rutile selected from two samples (E0814 and E0901) (Table 2) by the same technique.

The analytical results for four samples show that the zircon grains have highly variable uranium (142–1894 ppm) and thorium (129–3750 ppm) concentrations, as well as rather high Th/U ratios (0.84–2.26, Table 1). Four samples gave $^{206}\text{Pb}/^{238}\text{U}$ weighted mean ages of 237 ± 2 , 236 ± 3 , 236 ± 3 and 232 ± 3 Ma (Fig. 4). The analyzed 46 rutile grains from two samples (E0814 and E0901) are about 150 μm in size (diameter). They have low U contents ranging from 0.18 to 0.92 ppm, and high and variable proportions of common lead ($f_{206} = 4\text{--}93\%$) (Table 2). In the Tera–Wasserburg plot (Fig. 5), the linear regression of the data points gave two lower intercept ages of 218 ± 10 Ma and 217 ± 12 Ma for sample E0814 and E0901, respectively. The weighted mean $^{206}\text{Pb}/^{238}\text{U}$ ages are identical within the error limits, at 216 ± 9 Ma and 215 ± 11 Ma, using the ^{207}Pb -based common-lead correction.

Trace element and oxygen isotopic compositions

Zircon trace element and oxygen analyses were performed on the same spots as those for U–Pb dating. Eighty-three trace element analyses of zircon grains from four dated eclogite samples show a rather uniform composition (Supplementary Material 2). The chondrite-normalized REE patterns (Fig. 6) are characterized by moderate enrichment in heavy REE ($\text{Lu}_\text{N}/\text{Sm}_\text{N} = 14\text{--}41$), significantly negative Eu anomalies ($\text{Eu}/\text{Eu}^* = 0.14\text{--}0.43$) and positive Ce anomalies. The 89 zircon grains from four samples give $\delta^{18}\text{O}$ value of $+3.89\text{‰}$ to $+5.80\text{‰}$ (Table 1; Fig. 7). This result is outside the normal mantle $\delta^{18}\text{O}$ value of $+5.3 \pm 0.3\text{‰}$ (Valley 2003).

Table 2 SIMS U–Pb data for rutiles from the Qiangtang eclogite

Sample spot	U (ppm)	f_{206} (%)	$^{238}\text{U}/^{206}\text{Pb}$	$\pm\sigma$ (%)	$^{207}\text{Pb}/^{206}\text{Pb}$	$\pm\sigma$ (%)	$t_{206/238}$ (Ma)	$\pm\sigma$ (Ma)
E0814, eclogite								
E0814-1	0.5	4	29.3	8.1	0.077	16	209	17
E0814-2	0.29	7	25.3	7.9	0.103	15	234	19
E0814-3	0.32	74	8.7	8.5	0.625	5	200	38
E0814-4	0.49	6	30.4	7.1	0.096	14	197	14
E0814-5	0.31	11	25.5	8.8	0.133	14	223	20
E0814-6	0.24	12	25.5	9.0	0.140	19	221	21
E0814-7	0.40	31	22.1	11.7	0.294	11	199	26
E0814-8	0.36	15	26.3	8.0	0.163	14	207	18
E0814-9	0.56	4	26.3	6.7	0.080	14	232	16
E0814-10	0.59	18	25.8	6.3	0.187	9.3	203	14
E0814-11	0.55	5	28.5	7.3	0.090	14	211	16
E0814-12	0.37	56	13.9	7.9	0.486	7.3	206	28
E0814-13	0.25	88	5.7	12.6	0.738	6.4	146	78
E0814-14	0.46	6	25.3	8.0	0.096	17	236	19
E0814-15	0.42	9	24.9	8.0	0.119	15	232	19
E0814-16	0.5	9	26.1	7.2	0.118	15	222	17
E0814-17	0.26	19	24.4	10.6	0.196	22	212	26
E0814-18	0.92	21	23.3	8.4	0.210	9.4	217	19
E0814-19	0.36	74	5.9	6.2	0.631	5	284	54
E0901, eclogite								
E0901-1	0.39	77	5.03	12.1	0.650	4.7	292	61
E0901-2	0.57	84	4.04	15.3	0.709	3.3	247	61
E0901-3	0.4	10	28	9.3	0.127	16	204	20
E0901-4	0.32	84	4.28	7.1	0.703	4.5	243	64
E0901-5	0.3	89	3.21	12.7	0.741	4.9	229	97
E0901-6	0.55	14	25.7	7.7	0.156	11	213	17
E0901-7	0.22	90	3.03	11.9	0.751	3.9	216	86
E0901-8	0.23	90	2.43	8.1	0.753	5	263	130
E0901-9	0.25	85	3.93	11.0	0.712	5.1	247	81
E0901-10	0.33	82	5.93	9.3	0.686	4.8	199	50
E0901-11	0.21	85	5.49	10.5	0.712	6.5	177	71
E0901-12	0.22	92	3.79	7.4	0.768	4.5	138	78
E0901-13	0.28	80	6.75	9.2	0.672	5.5	192	48
E0901-14	0.25	93	2.51	16.7	0.772	3.7	195	101
E0901-15	0.41	89	3.17	12.8	0.747	5.3	217	106
E0901-16	0.3	31	20.5	9.7	0.294	14	213	26
E0901-17	0.33	92	4.01	13.7	0.771	4.2	124	70
E0901-18	0.55	16	28.6	11.6	0.172	12	188	22
E0901-19	0.18	88	3.37	8.5	0.735	4.7	233	87
E0901-20	0.57	10	24.6	6.1	0.131	11	231	15
E0901-21	0.26	89	2.82	7.4	0.744	3.5	253	80
E0901-22	0.52	7	28.9	7.3	0.104	15	204	15
E0901-23	0.37	73	8.75	9.4	0.617	5.5	200	37
E0901-24	0.27	8	25.5	11.4	0.114	20	228	27
E0901-25	0.69	7	26	8.0	0.106	13	227	18
E0901-26	0.44	10	27.6	9.0	0.129	18	207	20
E0901-27	0.37	11	24	10.0	0.137	16	234	24

Discussion

The timing of HP metamorphism

Mineral inclusions are the most powerful and direct way to discriminate the genesis of zircon from the HP metamorphic rocks (e.g., Hermann et al. 2001; Hoskin and Schaltegger 2003; Rubatto and Hermann 2007; Liu and Liou 2011). The zircon grains from the Qiangtang eclogite contain typical eclogite-facies assemblages. Furthermore, the inclusion relationships indicate that they are primary inclusions, and they should be trapped during the growth of zircon. That is, zircons from the Qiangtang eclogite were formed under the eclogite-facies conditions. In this study, we obtained zircon U–Pb ages of 232–237 Ma, which are identical with the Lu–Hf mineral isochron ages of 233–244 Ma (Pullen et al. 2008). Furthermore, these ages are indistinguishable from the zircon ages reported by Zhai et al. (2013b; 230–237 Ma). These ages should represent the time of the peak eclogite-facies metamorphism of the Qiangtang eclogite.

Rutile is a common accessory phase in eclogite, and it also records the time of high-pressure metamorphism. The closure temperature (T_c) for the rutile U–Pb system is lower than that of zircon. Field studies indicated that T_c of rutile was 400–500 °C at a grain radius of 90–210 μm (Mezger et al. 1989), similar to that of T_c of the phengite Ar–Ar age (ca. 400 °C; Hames and Bowring 1994; Harrison et al. 2009). Therefore, the rutile U–Pb age probably represents the time when the Qiangtang eclogite cooled down to 400–500 °C. In this study, a pooled analysis of all 46 measurements from two samples gave a lower intercept age of 217 ± 7 Ma (MSWD = 0.52) in the Tera–Wasserburg diagram (Fig. 5); this is considered as the best estimate for the rutile U–Pb age. This age agrees with the phengite Ar–Ar age of 214–219 Ma (Li et al. 2006a; Zhai et al. 2011b), and they date the cooling (exhumation) of the Qiangtang eclogite below ~ 500 °C.

Broadly, there is an interval between the peak eclogite-facies metamorphism and exhumation time, which is comparable with that of the HP–UHP rocks from the Dabie–Sulu orogen of eastern China (Liou et al. 2009; Liu and Liou 2011; Zheng 2012).

Unusual metamorphic zircons

In general, metamorphic zircon can usually be distinguished from magmatic zircon. Metamorphic zircon grains typically contain metamorphic mineral inclusions; they show irregular shape and internal structure, low Th/U ratios, and relatively flat heavy REE pattern for

garnet-bearing eclogite or amphibolite (e.g., Hoskin and Black 2000; Rubatto 2002; Corfu et al. 2003; Hoskin and Schaltegger 2003). The inclusion assemblage of omphacite, phengite, garnet and rutile indicates that the zircon of the Qiangtang eclogite was undoubtedly at the eclogite-facies conditions. Furthermore, the similarity in composition between the inclusions and matrix minerals (omphacite, phengite and garnet) suggests crystallization of zircon during prograde eclogite-facies metamorphism. However, the Qiangtang zircon grains show some unusual features for metamorphic zircon, that is, their euhedral habit, high Th/U ratios and enriched heavy REE patterns (Fig. 6).

Similar cases have been observed for metamorphic zircon from veins associated with eclogite in the Western Alps (Rubatto et al. 1999; Rubatto and Hermann 2003) and Dabie orogens (Zheng et al. 2007; Wu et al. 2009). Indeed, the high Th/U ratios of the zircon grains (0.84–2.26, Table 1) are unusual, but several similar cases have been reported from high-grade metamorphic rocks (granulite and eclogite) in the Alps and Himalaya orogenic belt (e.g., Vavra et al. 1999; Zhai et al. 2011b; Zhang et al. 2014). These rocks are mostly formed in subduction zones, where the metamorphic fluids would be enriched in some trace elements during subduction of the oceanic crust, and the zircon could be formed during the formation of eclogite and blueschist.

The negative Eu anomalies in zircon could either be inherited from the host rock or be the product of concurrent crystallization from the fluid when precipitating plagioclase (Rubatto 2002). The whole-rock geochemical data of the Qiangtang eclogite do not display any Eu anomaly (Zhai et al. 2011a), so that the negative Eu anomaly in the zircon could be attributed to the latter cause. That is, these zircon grains were most likely crystallized in the presence of plagioclase. The inclusion relationships argue for the coeval formation of zircon, omphacite, phengite, garnet and rutile, whereas the zircons show a steep HREE pattern, suggesting that the heavy REE abundances were not affected by the formation of garnet. Therefore, the zircon and garnet should be formed in where no trace element equilibrium between zircon and garnet was achieved. This prevented any change in zircon composition due to the crystallization of garnet or other minerals. Note that the Qiangtang eclogite was derived from oceanic crust of the Paleo-Tethys Ocean (Zhai et al. 2011a, b), and thus the metamorphic fluid would provide trace elements that could enter to the HP eclogites. Finally, the zircon $\delta^{18}\text{O}$ values of 3.89 to 5.80‰ for the zircon grains also argue for seawater-hydrothermal alteration for eclogite protolith, consistent with the oceanic origin of the Qiangtang eclogites (Zhai et al. 2011a, b).

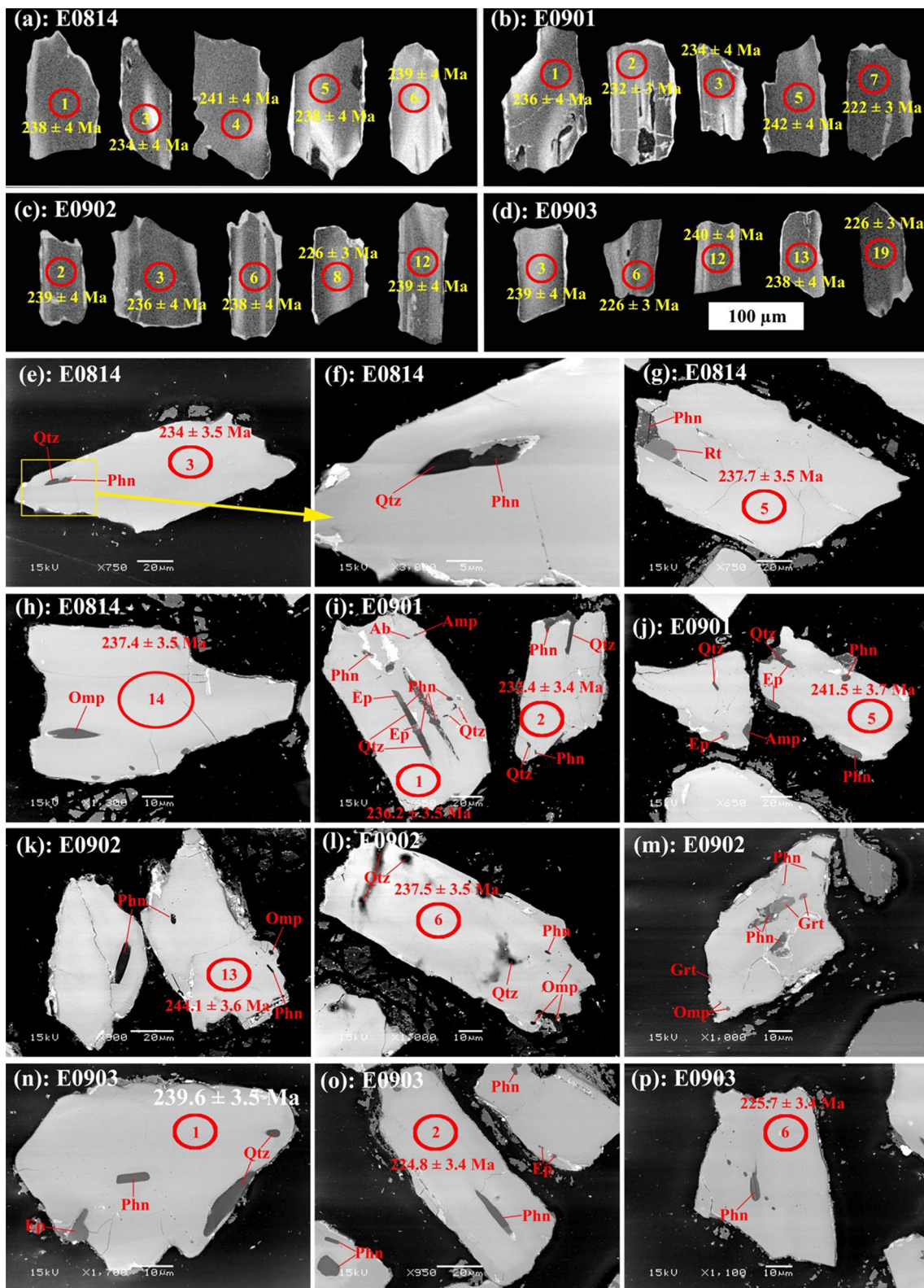


Fig. 3 a–d CL images showing the internal structures of zircon from the Qiangtang eclogites; e–p backscattered electron images showing inclusions in zircon

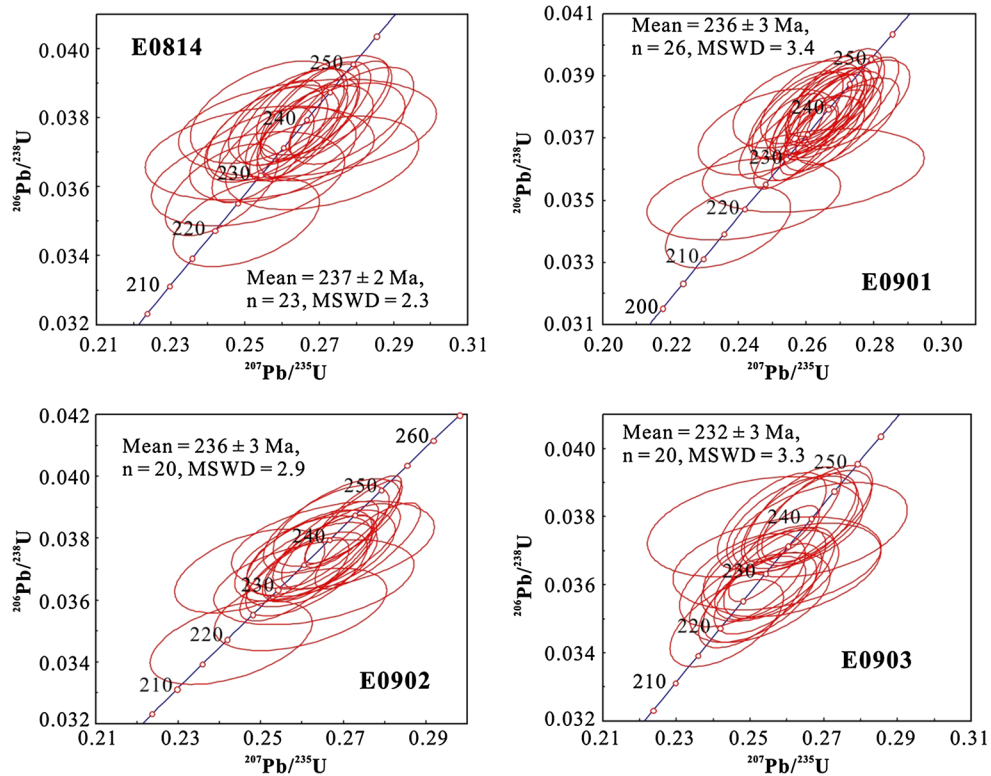


Fig. 4 SIMS zircon U–Pb concordia diagrams of the Qiangtang eclogite, northern Tibet

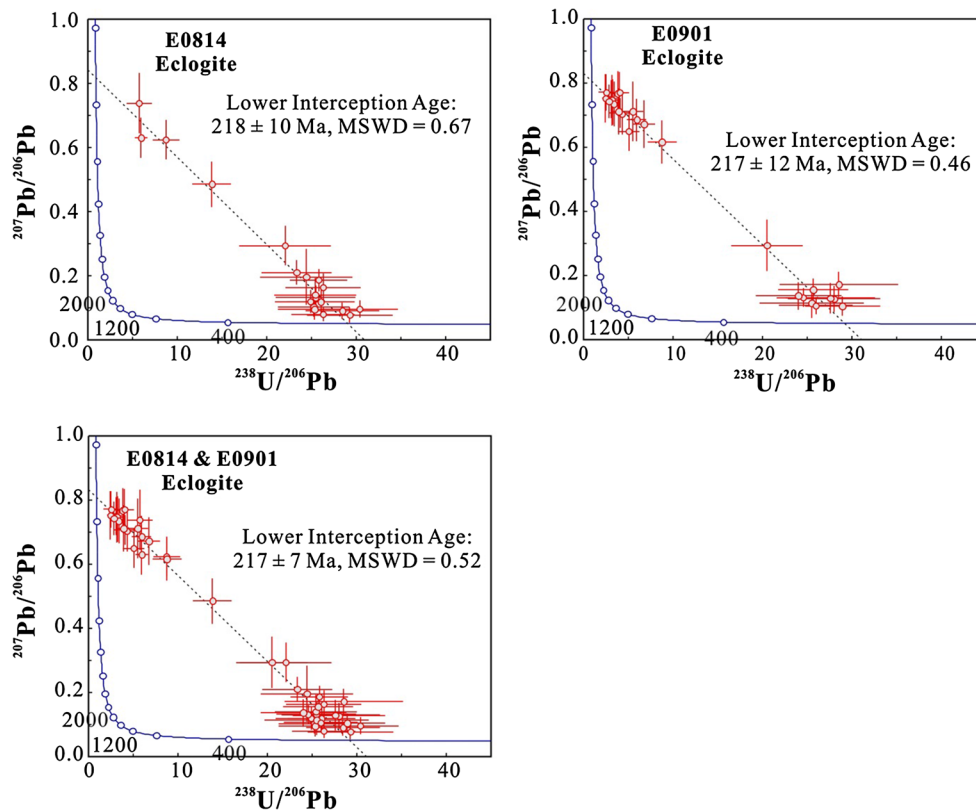


Fig. 5 U–Pb age concordia diagram for rutile from the Qiangtang eclogite

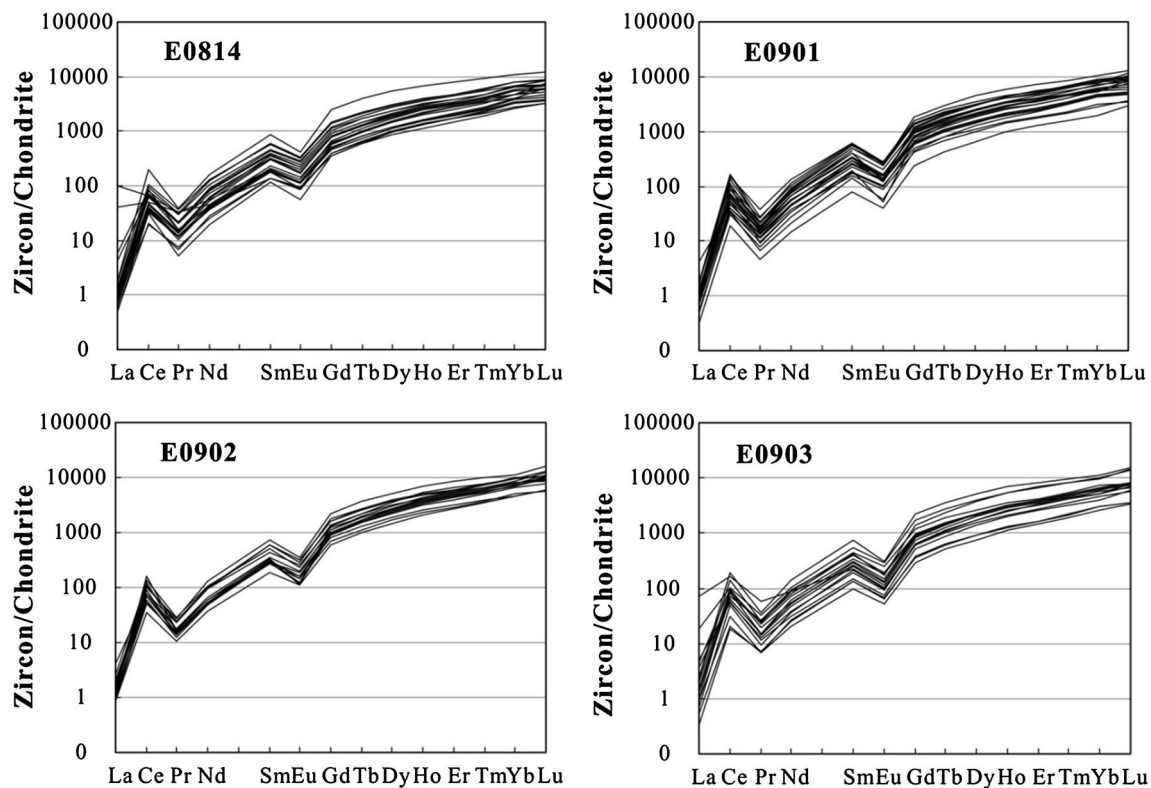


Fig. 6 Chondrite-normalized REE patterns of zircon from the Qiangtang eclogite. Chondrite and primitive mantle values are from Sun and McDonough (1989)

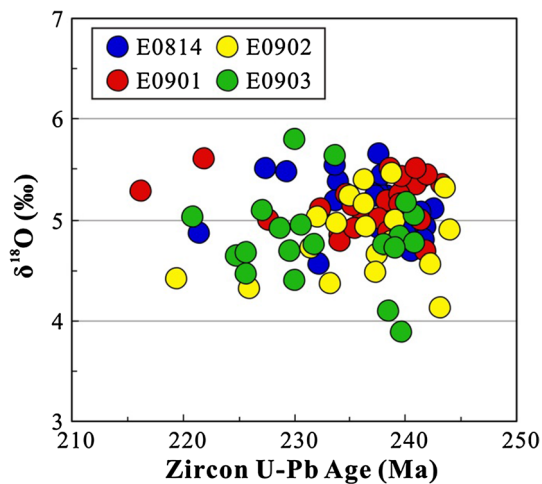


Fig. 7 $\delta^{18}\text{O}$ values versus ages of zircons from the Qiangtang eclogite

Tectonic evolution of the Qiangtang HP metamorphic belt

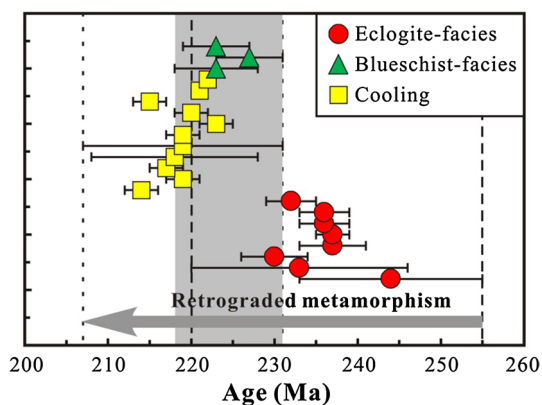
The Qiangtang HP metamorphic belt and associated ophiolitic mélanges marked a Paleo-Tethyan suture zone in the middle of the Qiangtang terrane, and it was recently

documented and hotly studied (Kapp et al. 2003; Li et al. 2006a, b; Pullen et al. 2008, 2011; Pullen and Kapp 2014; Zhai et al. 2011a, b, 2013a, b, c, 2016; Liang et al. 2012; Metcalfe 2013; Zhang et al. 2016). According to the newly published data, the ages of ophiolitic mélanges from this suture zone range from Middle Cambrian to Permian (Zhai et al. 2013a, 2016), and thus the Paleo-Tethys Ocean could open in the Middle Cambrian (Zhai et al. 2016). However, the close of this ocean is still unclear.

In generally, low-temperature/HP metamorphic rocks were formed by the oceanic subduction (e.g., Maruyama et al. 1996; Ernst 2001; Agard et al. 2009), and the Qiangtang eclogite and blueschist recorded the processes of the subduction and closure of the Paleo-Tethys Ocean. Table 3 and Fig. 8 are a summary for the ages of the HP metamorphic rocks in the Qiangtang area. We suggest that the time of the peak eclogite-facies metamorphism focused on a variation of 230–237 Ma inferred from the zircon U–Pb ages (Zhai et al. 2011b; this study). The Lu–Hf mineral isochron ages (233 ± 13 Ma and 244 ± 11 Ma) are similar to these ages (Pullen et al. 2008). Furthermore, there are only three ages for the blueschist-facies metamorphism, that is, two glaucophane Ar–Ar ages (Li 1997; Zhai et al. 2009) and one Lu–Hf mineral isochron age (Pullen et al. 2008) (Table 3). These ages are similar and display a narrow

Table 3 Summary of age data for the HP metamorphic rocks in the Qiangtang area

Location	Lithology	Dating methods	Age (Ma)	References
Gemu	Eclogite	Lu–Hf isochron	244 ± 11 Ma	Pullen et al. (2008)
Gemu	Eclogite	Lu–Hf isochron	233 ± 13 Ma	Pullen et al. (2008)
Gemu	Eclogite	Zircon LA-ICPMS U–Pb	230 ± 4 Ma	Zhai et al. (2011b)
Gemu	Eclogite	Zircon SHRIMP U–Pb	237 ± 4 Ma	Zhai et al. (2011b)
Gemu	Eclogite	Zircon SIMS U–Pb	237 ± 2 Ma	This study
Gemu	Eclogite	Zircon SIMS U–Pb	236 ± 3 Ma	This study
Gemu	Eclogite	Zircon SIMS U–Pb	236 ± 3 Ma	This study
Gemu	Eclogite	Zircon SIMS U–Pb	232 ± 3 Ma	This study
Gemu	Eclogite	Phengite Ar–Ar	214 ± 2 Ma	Zhai et al. (2011b)
Gemu	Eclogite	Phengite Ar–Ar	219 ± 2 Ma	Li et al. (2006a)
Gemu	Eclogite	Phengite Ar–Ar	217 ± 2 Ma	Li et al. (2006a)
Gemu	Eclogite	Rutile SIMS U–Pb	218 ± 10 Ma	This study
Gemu	Eclogite	Rutile SIMS U–Pb	219 ± 12 Ma	This study
Gemu	Phengite schist	Phengite Ar–Ar	219 ± 2 Ma	Dong et al. (2009)
Gemu	Garnet–phengite schist	Phengite Ar–Ar	223 ± 2 Ma	Zhai et al. (2011b)
Gangma Co	Eclogite	Phengite Ar–Ar	220 ± 2 Ma	Zhai et al. (2011b)
Rongma	Blueschist	Lu–Hf isochron	223 ± 5 Ma	Pullen et al. (2008)
Rongma	Blueschist	Glaucophane Ar–Ar	227 ± 4 Ma	Zhai et al. (2009)
Rongma	Blueschist	Phengite Ar–Ar	215 ± 2 Ma	Zhai et al. (2009)
Rongma	Blueschist	Phengite Ar–Ar	221 ± 0.3 Ma	Kapp et al. (2003)
Rongma	Blueschist	Phengite Ar–Ar	222 ± 0.1 Ma	Kapp et al. (2003)
Shuanghu	Blueschist	Glaucophane Ar–Ar	223 ± 4 Ma	Li (1997)

**Fig. 8** Age data for the HP metamorphic rocks in the Qiangtang area. Data sources: Li (1997); Kapp et al. (2003); Li et al. (2006a); Pullen et al. (2008); Dong et al. (2009); Zhai et al. (2009, 2011b); This study. See Table 3 for details

range (223–227 Ma), and they are interpreted as the timing of the decompression blueschist stage (Zhai et al. 2011b). The cooling time of the HP metamorphic rocks was constrained by phengite and rutile from eclogite and garnet–phengite schist. Their ages mainly range from 214 to 223 Ma (Table 3), and they represent the cooling time of these HP metamorphic rocks.

In conclusion, the peak eclogite-facies stage (223–227 Ma) represented the oceanic subduction of the

Paleo-Tethys Ocean in the middle of the Qiangtang area, whereas the cooling stage (greenschist-facies; 214–223 Ma) recorded the final exhumation of the HP metamorphic rocks. Furthermore, the blueschist-facies stage (223–227 Ma) is the result of the decompression of the HP metamorphic rocks during their exhumation. Therefore, the ages of these HP metamorphic rocks display a tectonic evolution of the Qiangtang HP metamorphic belt from oceanic subduction to exhumation in the Middle-Late Triassic.

Conclusions

Our new data suggest that: (1) the timing of the peak eclogite-facies and exhumation stages of the Qiangtang eclogite was 232–237 Ma and ca. 217 Ma, respectively; (2) zircon from the Qiangtang eclogite was metamorphic origin, even though it has high Th/U ratios and enriched heavy REE compositions. The apparent paradox could be explained whereby the zircon grains crystallized from a different reservoir from that for garnet where no trace element was present and trace element equilibrium between zircon and garnet was achieved. (3) We caution that zircon grains of metamorphic and magmatic origins cannot be always distinguished by the criteria of Th/U ratio and heavy REE patterns for the HP–UHP metamorphic rocks of oceanic derivation. (4) The ages

of the HP metamorphic rocks display a tectonic evolution of the Qiangtang HP metamorphic belt from oceanic subduction to exhumation in the Middle-Late Triassic.

Acknowledgements We thank Zhen-yu Chen, Li Su, Yu Liu and Guo-qiang Tang for help with the laboratory work. We also thank Prof. J. G. Liou and another anonymous reviewer for their constructive reviews and Prof. Wolf-Christian Dullo and Wen-jiao Xiao for careful editorial handling. This study was supported by the Ministry of Science and Technology of China (2016YFC0600304), National Natural Science Foundation of China (Grant Nos. 41522204 and 41502216) and Chinese Geological Survey Project (Grant No. DD20160123-05). Bor-ming Jahn acknowledges financial support from the National Science Council (Taiwan) through grants NSC 100-2116-M-002-024.

References

- Agard P, Yamato P, Jolivet L, Burov E (2009) Exhumation of oceanic blueschists and eclogites in subduction zones: timing and mechanisms. *Earth-Sci Rev* 92(1–2):53–79
- BGMR (Bureau of Geology and Mineral Resources of Xizang Autonomous Region) (1993) Regional geology of Xizang (Tibet) Autonomous Region. Geological Publishing House, Beijing (in Chinese with English abstract)
- Black LP, Kamo SL, Allen CM, Davis DW, Aleinikoff JN, Valley JW, Mundil R, Campbell IH, Korsch RJ, Williams IS, Foudoulis C (2004) Improved $^{206}\text{Pb}/^{238}\text{U}$ microprobe geochronology by the monitoring of a trace-element-related matrix effect; SHRIMP, ID-TIMS, ELA-ICP-MS and oxygen isotope documentation for a series of zircon standards. *Chem Geol* 205(1–2):115–140
- Cawthorn RG, Collerson KD (1974) Recalculation of pyroxene end-member parameters and estimation of ferrous and ferric iron content from electron-microprobe analyses. *Am Mineral* 59(11–1):1203–1208
- Clark DJ, Hensen BJ, Kinny PD (2000) Geochronological constraints for a two-stage history of the Albany-Fraser Orogen, Western Australia. *Precambrian Res* 102(3–4):155–183
- Corfu F, Hanchar JM, Hoskin PWO, Kinny P (2003) Atlas of Zircon Textures. *Rev Mineral Geochem* 53(1):469–500
- Dong YS, Li C, Shi JR, Wang SY (2009) Retrograde metamorphism and tectonic emplacement of high pressure metamorphic belt in central Qiangtang, Tibet. *Acta Petrol Sin* 25(9):2303–2309 (in Chinese with English abstract)
- Droop GTR (1987) A general equation for estimating Fe³⁺ concentrations in ferromagnesian silicates and oxides from microprobe analyses, using stoichiometric criteria. *Mineral Mag* 51(361):431–435
- Ernst WG (2001) Subduction, ultrahigh-pressure metamorphism, and regurgitation of buoyant crustal slices—implications for arcs and continental growth. *Phys Earth Planet In* 127(1–4):253–275
- Gebauer D (1996) A P–T–t path for an (ultra?) high-pressure ultramafic/mafic rock-association and its felsic country-rocks based on SHRIMP-dating of magmatic and metamorphic zircon domains. example: Alpe Arami (Central Swiss Alps). In: *Earth Processes: Reading the Isotopic Code*, vol. American Geophysical Union, pp 307–329
- Hames WE, Bowring SA (1994) An empirical-evaluation of the argon diffusion geometry in muscovite. *Earth Planet Sc Lett* 124(1–4):161–167
- Harrison TM, Célérier J, Aikman AB, Hermann J, Heizler MT (2009) Diffusion of ^{40}Ar in muscovite. *Geochim Cosmochim Acta* 73(4):1039–1051
- Hermann J, Rubatto D, Korsakov A, Shatsky VS (2001) Multiple zircon growth during fast exhumation of diamondiferous, deeply subducted continental crust (Kokchetav Massif, Kazakhstan). *Contrib Mineral Petr* 141(1):66–82
- Hoskin PWO, Black LP (2000) Metamorphic zircon formation by solid-state recrystallization of protolith igneous zircon. *J Metamorph Geol* 18(4):423–439
- Hoskin PWO, Schaltegger U (2003) The Composition of Zircon and Igneous and Metamorphic Petrogenesis. *Rev Mineral Geochem* 53(1):27–62
- Ireland TR, Williams IS (2003) Considerations in zircon geochronology by SIMS. *Rev Mineral Geochem* 53(1):215–241
- Jin XC (2002) Permo-carboniferous sequences of Gondwana affinity in southwest China and their paleogeographic implications. *J Asian Earth Sci* 20(6):633–646
- Kapp P, Yin A, Manning CE, Harrison TM, Taylor MH, Ding L (2003) Tectonic evolution of the early Mesozoic blueschist-bearing Qiangtang metamorphic belt, central Tibet. *Tectonics* 22(4):1043
- Kretz R (1983) Symbols for rock-forming minerals. *Am Mineral* 68(1–2):277–279
- Li C (1997) The $^{40}\text{Ar}/^{39}\text{Ar}$ age and its significance of the crossite from the blueschists in the mid-Qiangtang area, Tibet. *Chinese Sci Bull* 42:88
- Li C, Zheng A (1993) Paleozoic stratigraphy in the Qiangtang region of Tibet: relations of the Gondwana and Yangtze continents and ocean closure near the end of the carboniferous. *Int Geol Rev* 35(9):797–804
- Li C, Cheng LR, Hu K, Yang ZR, Hong YR (1995) Study on the Paleo-Tethys suture zone of Lungmu Co-Shuanghu. Geological Publishing House, Beijing (in Chinese with English abstract)
- Li QL, Li SG, Zheng YF, Li HM, Massonne HJ, Wang QC (2003) A high precision U–Pb age of metamorphic rutile in coesite-bearing eclogite from the Dabie Mountains in central China: a new constraint on the cooling history. *Chem Geol* 200(3–4):255–265
- Li C, Zhai QG, Chen W, Yu JJ, Huang XP, Zhang Y (2006a) Ar–Ar chronometry of the eclogite from central Qiangtang area, Qinghai-Tibet Plateau. *Acta Petrol Sin* 22(12):2843–2849 (in Chinese with English abstract)
- Li C, Zhai QG, Dong YS, Huang XP (2006b) Discovery of eclogite and its geological significance in Qiangtang area, central Tibet. *Chinese Sci Bull* 51(9):1095–1100
- Li XH, Liu Y, Li QL, Guo CH, Chamberlain KR (2009) Precise determination of Phanerozoic zircon Pb/Pb age by multicollector SIMS without external standardization. *Geochem Geophys Geosyst* 10(4):Q04010
- Li QL, Li XH, Liu Y, Tang GQ, Yang JH, Zhu WG (2010a) Precise U–Pb and Pb–Pb dating of Phanerozoic baddeleyite by SIMS with oxygen flooding technique. *J Anal Atom Spectrom* 25(7):1107–1113
- Li QL, Li XH, Liu Y, Wu FY, Yang JH, Mitchell RH (2010b) Precise U–Pb and Th–Pb age determination of kimberlitic perovskites by secondary ion mass spectrometry. *Chem Geol* 269(3–4):396–405
- Li XH, Li WX, Li QL, Wang XC, Liu Y, Yang YH (2010c) Petrogenesis and tectonic significance of the ~850 Ma Gangbian alkaline complex in South China: evidence from in situ zircon U–Pb dating, Hf–O isotopes and whole-rock geochemistry. *Lithos* 114(1–2):1–15
- Li QL, Lin W, Su W, Li XH, Shi YH, Liu Y, Tang GQ (2011) SIMS U–Pb rutile age of low-temperature eclogites from southwestern Chinese Tianshan, NW China. *Lithos* 122(1–2):76–86
- Liang X, Wang G, Yuan G, Liu Y (2012) Structural sequence and geochronology of the Qomo Ri accretionary complex, Central Qiangtang, Tibet: implications for the Late Triassic subduction of the Paleo-Tethys Ocean. *Gondwana Res* 22(2):470–481

- Liou JG, Ernst WG, Zhang RY, Tsujimori T, Jahn BM (2009) Ultra-high-pressure minerals and metamorphic terranes—The view from China. *J Asian Earth Sci* 35(3–4):199–231
- Liu FL, Liou JG (2011) Zircon as the best mineral for P-T-time history of UHP metamorphism: a review on mineral inclusions and U-Pb SHRIMP ages of zircons from the Dabie-Sulu UHP rocks. *J Asian Earth Sci* 40(1):1–39
- Ludwig KR (2001) *Squid1.02: A user's manual*. Berkeley Geochronological Center Special Publication, No. 2, 19
- Luvizotto GL, Zack T, Meyer HP, Ludwig T, Triebold S, Kronz A, Munker C, Stockli DF, Prowatke S, Klemme S, Jacob DE, von Eynatten H (2009) Rutile crystals as potential trace element and isotope mineral standards for microanalysis. *Chem Geol* 261(3–4):346–369
- Maruyama S, Liou J, Terabayashi M (1996) Blueschists and eclogites of the world and their exhumation. *Int Geol Rev* 38(6):485–594
- Metcalfe I (2013) Gondwana dispersion and Asian accretion: tectonic and palaeogeographic evolution of eastern Tethys. *J Asian Earth Sci* 66:1–33
- Mezger K, Hanson GN, Bohlen SR (1989) High-precision UPb ages of metamorphic rutile: application to the cooling history of high-grade terranes. *Earth Planet Sc Lett* 96(1–2):106–118
- Pullen A, Kapp P (2014) Mesozoic tectonic history and lithospheric structure of the Qiangtang terrane: insights from the Qiangtang metamorphic belt, central Tibet. *Geol Soc Am Special Papers* 507:71–87
- Pullen A, Kapp P, Gehrels GE, Vervoort JD, Ding L (2008) Triassic continental subduction in central Tibet and Mediterranean-style closure of the Paleo-Tethys Ocean. *Geology* 36(5):351–354
- Pullen A, Kapp P, Gehrels GE, Ding L, Zhang Q (2011) Metamorphic rocks in central Tibet: lateral variations and implications for crustal structure. *Geol Soc Am Bull* 123(3–4):585–600
- Robinson D, Spear FS, Schumacher JC (1982) Phase relations of metamorphic amphiboles: natural occurrence and theory. In: Veblen DR, Ribbe PH (eds) *Amphiboles, petrology and experimental phase relations, reviews of mineralogy, vol 9b.*, Mineralogical Society of America Washington, DC, pp 1–227
- Rowley DB, Xue F, Tucker RD, Peng ZX, Baker J, Davis A (1997) Ages of ultrahigh pressure metamorphism and protolith orthogneisses from the eastern Dabie Shan: *u/Pb* zircon geochronology. *Earth Planet Sc Lett* 151(3–4):191–203
- Rubatto D (2002) Zircon trace element geochemistry: partitioning with garnet and the link between U–Pb ages and metamorphism. *Chem Geol* 184(1–2):123–138
- Rubatto D, Hermann J (2003) Zircon formation during fluid circulation in eclogites (Monviso, Western Alps): implications for Zr and Hf budget in subduction zones. *Geochim Cosmochim Acta* 67(12):2173–2187
- Rubatto D, Hermann J (2007) Zircon behaviour in deeply subducted rocks. *Elements* 3(1):31–35
- Rubatto D, Gebauer D, Compagnoni R (1999) Dating of eclogite-facies zircons: the age of Alpine metamorphism in the Sesia-Lanzo Zone (Western Alps). *Earth Planet Sc Lett* 167(3–4):141–158
- Shi G, Li X, Li Q, Chen Z, Deng J, Liu Y, Kang Z, Pang E, Xu Y, Jia X (2012) Ion Microprobe U–Pb Age and Zr-in-Rutile thermometry of rutiles from the Daixian rutile deposit in the Hengshan Mountains, Shanxi Province, China. *Econ Geol* 107(3):525–535
- Stacey JS, Kramers JD (1975) Approximation of terrestrial lead isotope evolution by a two-stage model. *Earth Planet Sc Lett* 26(2):207–221
- Sun SS, McDonough WF (1989) Chemical and isotopic systematics of oceanic basalts: implications for mantle composition and processes. *Geol Soc Lond Special Publ* 42:313–345
- Valley JW (2003) Oxygen isotopes in zircon. *Rev Mineral Geochem* 53(1):343–385
- Vavra G, Schmid R, Gebauer D (1999) Internal morphology, habit and U-Th-Pb microanalysis of amphibolite-to-granulite facies zircons: geochronology of the Ivrea Zone (Southern Alps). *Contrib Mineral Petr* 134(4):380–404
- Wiedenbeck M, Allé P, Corfu F, Griffin WL, Meier M, Oberli F, Quadt AV, Roddick JC, Spiegel W (1995) Three natural zircon standards for U–Th–Pb, Lu–Hf, trace element and REE analyses. *Geostandard Newslett* 19(1):1–23
- Wiedenbeck M, Hancher JM, Peck WH, Sylvester P, Valley J, Whitehouse M, Kronz A, Morishita Y, Nasdala L, Fiebig J, Franchi I, Girard JP, Greenwood RC, Hinton R, Kita N, Mason PRD, Norman M, Ogasawara M, Piccoli PM, Rhede D, Satoh H, Schulz-Dobrick B, Skår O, Spicuzza MJ, Terada K, Tindle A, Togashi S, Vennemann T, Xie Q, Zheng YF (2004) Further characterisation of the 91500 zircon crystal. *Geostand Geoanal Res* 28(1):9–39
- Williams IS (1998) U–Th–Pb geochronology by ion microprobe. In: McKibben MA, Shanks WC, Ridley WI (eds) *Applications of microanalytical techniques to understanding mineralizing processes: Reviews in Economic Geology, vol 7.* pp 1–35
- Wu Y, Zheng Y (2004) Genesis of zircon and its constraints on interpretation of U–Pb age. *Chinese Sci Bull* 49(15):1554–1569
- Wu YB, Gao S, Zhang HF, Yang SH, Liu XC, Jiao WF, Liu YS, Yuan HL, Gong HJ, He MC (2009) U–Pb age, trace-element, and Hf-isotope compositions of zircon in a quartz vein from eclogite in the western Dabie Mountains: constraints on fluid flow during early exhumation of ultra high-pressure rocks. *Am Mineral* 94(2–3):303–312
- Yin A, Harrison TM (2000) Geologic evolution of the Himalayan-Tibetan orogen. *Annu Rev Earth Pl Sc* 28:211–280
- Zhai QG, Li C, Wang J, Chen W, Zhang Y (2009) Petrology, mineralogy and $^{40}\text{Ar}/^{39}\text{Ar}$ chronology for Rongma blueschist from central Qiangtang, northern Tibet. *Acta Petrol Sin* 25(9):2281–2288 **(in Chinese with English abstract)**
- Zhai QG, Jahn BM, Zhang RY, Wang J, Su L (2011a) Triassic Subduction of the Paleo-Tethys in northern Tibet, China: evidence from the geochemical and isotopic characteristics of eclogites and blueschists of the Qiangtang Block. *J Asian Earth Sci* 42(6):1356–1370
- Zhai QG, Zhang RY, Jahn BM, Li C, Song SG, Wang J (2011b) Triassic eclogites from central Qiangtang, northern Tibet, China: petrology, geochronology and metamorphic P–T path. *Lithos* 125(1–2):173–189
- Zhai QG, Jahn BM, Wang J, Su L, Mo XX, Wang KL, Tang SH, Lee HY (2013a) The Carboniferous ophiolite in the middle of the Qiangtang terrane, Northern Tibet: SHRIMP U–Pb dating, geochemical and Sr–Nd–Hf isotopic characteristics. *Lithos* 168:186–199
- Zhai QG, Jahn BM, Su L, Wang J, Mo XX, Lee HY, Wang KL, Tang SH (2013b) Triassic arc magmatism in the Qiangtang area, northern Tibet: zircon U–Pb ages, geochemical and Sr–Nd–Hf isotopic characteristics, and tectonic implications. *J Asian Earth Sci* 63:162–178
- Zhai QG, Jahn BM, Su L, Ernst RE, Wang KL, Zhang RY, Wang J, Tang SH (2013c) SHRIMP zircon U–Pb geochronology, geochemistry and Sr–Nd–Hf isotopic compositions of a mafic dyke swarm in the Qiangtang terrane, northern Tibet and geodynamic implications. *Lithos* 174:28–43
- Zhai QG, Jahn BM, Wang J, Hu PY, Chung SL, Lee HY, Tang SH, Tang Y (2016) Oldest Paleo-Tethyan ophiolitic mélange in the Tibetan Plateau. *Geol Soc Am Bull* 128(3–4):355–373
- Zhang YC, Yuan TX, Zhai QG (2009) A Preliminary report of the fieldtrip on the Carboniferous-Permian sequences in the north and south of the Longmuco-Shuanghu suture zone, Northern Tibet in May and June. *Permophiles* 53:5–7
- Zhang XZ, Dong YS, Li C, Deng MR, Zhang L, Xu W (2014) Silurian high-pressure granulites from Central Qiangtang, Tibet:

- constraints on early Paleozoic collision along the northeastern margin of Gondwana. *Earth Planet Sc Lett* 405:39–51
- Zhang YC, Shen SZ, Zhai QG, Zhang YJ, Yuan DX (2016) Discovery of a Sphaeroschwagerina fusuline fauna from the Raggyorcaka Lake area, northern Tibet: implications for the origin of the Qiangtang Metamorphic Belt. *Geol Mag* 153(3):537–543
- Zheng YF (2009) Fluid regime in continental subduction zones: petrological insights from ultrahigh-pressure metamorphic rocks. *J Geol Soc London* 166:763–782
- Zheng YF (2012) Metamorphic chemical geodynamics in continental subduction zones. *Chem Geol* 328:5–48
- Zheng YF, Gao TS, Wu YB, Gong B, Liu XM (2007) Fluid flow during exhumation of deeply subducted continental crust: zircon U–Pb age and O-isotope studies of a quartz vein within ultrahigh-pressure eclogite. *J Metamorph Geol* 25(2):267–283
- Zhu DC, Zhao ZD, Niu YL, Dilek Y, Hou ZQ, Mo XX (2013) The origin and pre-Cenozoic evolution of the Tibetan Plateau. *Gondwana Res* 23(4):1429–1454